Journal of
Composites Science

MDPI

Article

Modal-Based Identification of Equivalent Material Properties of 3D-Printed Lattice-Core Plates with Different Infill Levels

Róbert Huňady [1,2], Michal Fabian [1], Martin Hagara [1,*] and Peter Palička [3]

[1] Faculty of Mechanical Engineering, Technical University of Kosice, Letna 1/9, 042 00 Kosice, Slovakia; robert.hunady@tuke.sk (R.H.); michal.fabian@tuke.sk (M.F.)
[2] Faculty of Mechanical Engineering, VSB—Technical University of Ostrava, 17. Listopadu 2172/15, 708 00 Ostrava, Czech Republic
[3] Faculty of Aeronautics, Technical University of Kosice, Rampová 7, 041 21 Kosice, Slovakia; peter.palicka@tuke.sk
* Correspondence: martin.hagara@tuke.sk

Abstract

This study presents a modal-based approach for identifying the equivalent material properties of 3D-printed plates with lattice cores without requiring detailed modelling of their internal geometry. Plates with different core infill densities ranging from 20% to 100% were experimentally investigated by modal analysis and represented by a homogenized orthotropic model with square symmetry, characterized by three independent equivalent elastic constants: Young's modulus, Poisson's ratio, and shear modulus. These constants were identified by minimizing a weighted objective function combining discrepancies in natural frequencies and mode shapes quantified by the Modal Assurance Criterion, while the modal characteristics of the homogenized plates were calculated using the Ritz method. The identified models showed high agreement with the experimental modal characteristics across all investigated infill densities. Independent identification of the shear modulus enabled the twisting stiffness to be represented without the constraints imposed by isotropy, revealing a non-monotonic dependence of the deviation from isotropic constitutive behavior on core infill density. Comparison with independently optimized isotropic models confirmed that the additional elastic constant improves the prediction of natural frequencies and mode shapes, particularly at intermediate infill densities. Additional finite element analyses highlighted the limitations of using nominal material properties and demonstrated the substantially lower computational cost of the proposed identification approach compared with FE model updating. The methodology provides an efficient means of obtaining experimentally informed equivalent material properties for simplified dynamic modelling of 3D-printed lattice-core structures.

Keywords: 3D-printed plates; lattice core; homogenization; equivalent material properties; orthotropic material; experimental modal analysis; Ritz method; modal-based identification; independent shear modulus

Check for updates

Academic Editors: Haifeng Zhao, Konstantinos Tserpes and Salim Belouettar

Received: 8 October 2026
Revised: 12 November 2026
Accepted: 17 November 2026
Published: 19 November 2026

Copyright: © 2026 by the authors. Licensee MDPI, Basel, Switzerland. This article is an open access article distributed under the terms and conditions of the Creative Commons Attribution (CC BY) license.

1. Introduction

Additive manufacturing of polymer components has undergone significant development in recent years and is increasingly being applied to the production of lightweight structural components with complex geometries and purposefully designed internal structures. One of its major advantages is the possibility of modifying the mechanical properties of a component through manufacturing parameters and infill architecture without changing

the base material. However, the mechanical response of components produced by material extrusion technologies depends not only on the properties of the input polymer but also on process and geometric factors, such as print and layer orientation, raster arrangement, bonding between individual layers, layer thickness, infill density and geometry, and manufacturing imperfections. Sola et al. [1] highlighted the specific aspects of mechanical testing of additively manufactured polymers and showed that the measured tensile properties of FFF components can be affected by manufacturing parameters as well as by the geometry and dimensions of the test specimen. The influence of internal architecture on mechanical properties was confirmed by Harpool et al. [2], who investigated the tensile response of PLA specimens with different infill geometries, while Birosz et al. [3] analyzed the influence of infill type and density on the flexural response of FDM components. Therefore, the nominal material properties of the input polymer may not adequately represent the effective mechanical properties of the resulting printed structure, and its reliable analytical or numerical modeling requires parameters corresponding to the mechanical response of the actual manufactured structure.

This issue is particularly important for lattice structures, in which the macroscopic mechanical response is determined not only by the properties of the base material but also by the unit-cell topology, relative density, orientation of individual elements, and manufacturing process. Guo et al. [4] experimentally and numerically demonstrated the anisotropic mechanical response of additively manufactured polymer lattice structures and proposed a constitutive model taking into account the print orientation. Egan et al. [5] showed that the mechanical properties of polymer lattices are strongly influenced by topology, relative density, and manufacturing conditions. Further studies confirmed the considerable influence of cell architecture, relative density, and manufacturing-induced anisotropy on the direction-dependent mechanical response of both conventional and TPMS lattice structures [6–8].

Due to the interaction between the properties of the base material, the manufacturing process, and the internal architecture, the use of material parameters derived solely from the properties of the solid material can be problematic when numerically modeling lattice components. This is particularly important in explicit modeling of the internal lattice geometry within the framework of finite element analysis, where an appropriate definition of the material model and its parameters significantly affect the ability of the numerical model to reproduce the mechanical and dynamic response of the actual structure. Detailed modeling of larger lattice structures also complicates geometry and mesh generation and leads to a substantial increase in the number of degrees of freedom and computational cost, particularly in parametric studies, optimization, and repeated dynamic analyses. Homogenization therefore represents an attractive alternative in which the heterogeneous cellular architecture is replaced by an equivalent continuum characterized by effective material properties.

Numerical homogenization methods based on representative volume elements (RVEs) are widely used to determine the effective elastic properties of 3D-printed materials and cellular structures. Anoop and Senthil [9] used a microscopic RVE model to determine the effective elastic constants of FDM components, while taking into account the characteristics of their internal structure and manufacturing parameters. Gonabadi et al. [10] systematically evaluated the effects of raster angle, build orientation, and infill density through FE microstructural modeling and homogenization. Alternative numerical representations of FDM microstructures were employed by Bhandari and Lopez-Anido [11], who used lattice and shell FE models to predict the elastic constants of extrusion-based 3D-printed polymers and compared the results with experimental data. Bean et al. [12] used an RVE model with periodic boundary conditions to determine the effective elastic properties of 3D-printed

gyroid infills with different densities and experimentally validated selected numerical results. The computational cost of homogenizing complex 3D-printed microstructures can be further reduced using reduced-order models, as demonstrated by Monaldo and Marfia [13].

Homogenization methods have also been extended to the structural level of lattice and sandwich plates, where they allow the detailed cellular architecture to be replaced by an equivalent plate or shell model. Wu et al. [14] used an improved asymptotic homogenization method for the vibration analysis of composite sandwich plates with lattice grids. Guan et al. [15,16] developed RVE-based homogenization approaches for the dynamic analysis of sandwich panels, including pyramidal lattice-truss structures, and used the homogenized models to predict natural frequencies, mode shapes, and damping.

An alternative to the conventional experimental testing and forward homogenization procedures is inverse identification, in which the parameters of a material or equivalent constitutive model are determined based on the experimentally observed structural response. In this context, methods based on vibration data are particularly suitable because natural frequencies and mode shapes contain information about the global mass and stiffness properties of the structure and can be determined non-destructively. The relevance of experimental modal analysis for the characterization of 3D-printed polymer components was demonstrated by Nguyen et al. [17], proving the sensitivity of modal characteristics to manufacturing conditions. Beyond homogenization-based approaches, various numerical methods have been developed for the free-vibration analysis of structures with non-uniform geometry and material properties. For example, Baran [18] employed a Haar wavelet formulation with an auxiliary-function approach to analyze the free vibrations of non-uniform, functionally graded Timoshenko beams, demonstrating improved numerical accuracy and efficiency.

Vibration data have been used in various inverse formulations to identify the elastic properties of plate structures. Ablitzer et al. [19] identified the flexural stiffness parameters of orthotropic plates directly from vibration measurements using local dynamic equilibrium. Battaglia et al. [20] developed a vibration-based identification procedure combining the Rayleigh–Ritz formulation and Particle Swarm Optimization to estimate the elastic constants of orthotropic plates. Their approach employed an objective function based exclusively on discrepancies between experimental and calculated natural frequencies, while mode shapes were used for subsequent validation rather than being incorporated into the identification criterion. The method was also experimentally validated on 3D-printed stiffened plates, demonstrating its capability to identify equivalent orthotropic properties without repeated finite element analyses. De Nunzio et al. [21] combined experimental modal analysis, a Ritz model, and numerical optimization to identify the elastic constants and material orientation of 3D-printed PLA specimens and compared the identified values with those obtained from the quasi-static loading tests. Some studies have focused on improving the computational efficiency and robustness of inverse identification through Fourier-based [22] and pseudo-direct methods [23], as well as modifications to objective-function formulations aimed at reducing distortion in the identified elastic properties [24].

An alternative group comprises finite element model updating (FEMU) methods, in which the parameters of a numerical model are iteratively adjusted to reduce the discrepancy between calculated and experimentally determined modal characteristics. Cuadrado et al. [25] combined experimental modal analysis, sensitivity analysis, and gradient-based optimization to update material and model parameters of composite plates through FE models based on experimentally determined natural frequencies and mode shapes. Viala et al. [26] used vibration measurements in combination with FEMU for the inverse identification of anisotropic elastic and damping properties of a composite structure. In the field of additively manufactured polymers, Zhang et al. [27] combined modal data with Bayesian FE

model updating and a Random Forest surrogate model for the non-destructive identification of the equivalent elastic modulus of FDM components at reduced computational cost.

Despite these advances, the experimental identification of equivalent constitutive properties for complete 3D-printed lattice-core plates remains insufficiently investigated. Conventional homogenization approaches generally derive effective properties from the geometry and mechanical characteristics of representative cells, whereas vibration-based inverse identification methods have predominantly been applied to homogeneous, composite, or stiffened plates. Consequently, limited attention has been devoted to identifying the equivalent elastic response of complete lattice-core structures, accounting for the combined effects of face sheets, internal lattice architecture, and manufacturing-related deviations without explicitly modeling their internal geometry. In particular, the influence of core infill density on the equivalent constitutive properties and the adequacy of isotropic assumptions for reproducing the global dynamic response require further investigation.

To address these gaps, this study presents an experimental modal-based homogenization procedure for 3D-printed lattice-core plates with five different core infill densities. The heterogeneous structure is represented by a homogeneous orthotropic plate with square symmetry, characterized by three independently identified equivalent elastic constants: Young's modulus, Poisson's ratio, and shear modulus. The forward modal problem is solved using the Ritz method, while the equivalent properties are determined by minimizing a weighted objective function incorporating both natural-frequency discrepancies and mode-shape differences quantified by the Modal Assurance Criterion (MAC). By extending frequency-based identification to include mode-shape correlation, the proposed approach accounts for both the spectral and spatial characteristics of the measured dynamic response. The study further investigates the influence of core infill density on the identified elastic properties, evaluates the role of independently identified shear modulus in reproducing the effective twisting stiffness, and quantitatively compares isotropic and square-symmetric orthotropic representations. The proposed methodology is also evaluated against finite element models, including an explicitly modeled lattice-core structure and an equivalent model calibrated through FE model updating, to assess its predictive capability and computational efficiency. Particular emphasis is placed on revealing core-infill-density-dependent deviations from isotropic constitutive behavior and assessing their consequences for modal prediction. The resulting methodology provides a computationally efficient means of identifying experimentally informed equivalent material properties for simplified structural models without explicitly representing the internal lattice geometry.

2. Materials and Methods

2.1. 3D-Printed Lattice-Core Plates

The 3D-printed rectangular plates of constant thickness, composed of two solid face sheets and an internal core with a square lattice structure, are investigated in this study. The square cells of the core are oriented at an angle of 45° with respect to the principal axes x and y of the plate, with the core being enclosed around its entire perimeter by a solid frame. The internal structure created in this way represents a regular grid formed by mutually intersecting ribs. An ABS-based thermoplastic filament, Z-ULTRAT, was used as the base material, characterized by high strength, impact resistance, and minimal shrinkage. The reference mechanical properties of the material used to produce the specimens are listed in Table 1.

Table 1. Reference mechanical properties of Z-ULTRAT material [28].

Material Density [kg/m^3]	Tensile Modulus [MPa]	Poisson's Ratio [–]	Yield Strength [MPa]	Hardness (Rockwell) [–]	Linear Shrinkage [%]
1080	1950	0.35	42	110	0.5–0.8

The specimens were manufactured on a Zortrax M200 3D printer (Zortrax S.A., Olsztyn, Poland) using LPD (Layer Plastic Deposition) technology. The geometric configuration of the plates and the shape and orientation of the lattice core, including the basic 3D printing parameters, are shown in Figure 1. In total, five specimens were analyzed, differing in their core infill density, namely 20%, 40%, 60%, 80%, and 100%. The core infill density was specified as a printing parameter in the slicing software and represents the nominal percentage of core infill rather than the actual solid volume fraction of the lattice core. This parameter is used exclusively to distinguish between the investigated specimens and to characterize the manufacturing parameter by which they differ.

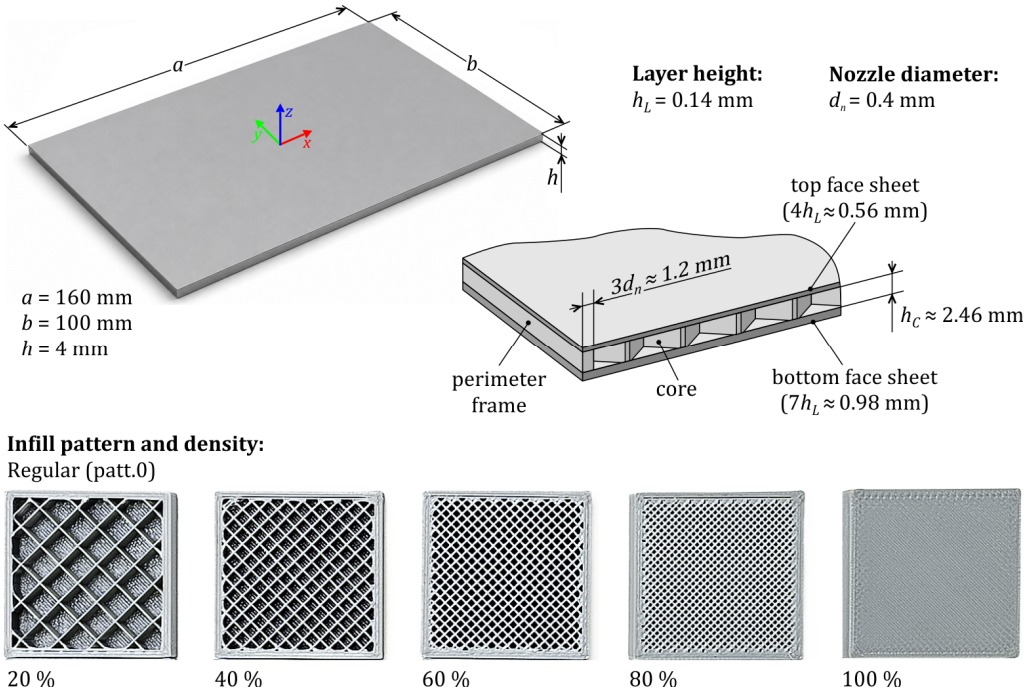

Figure 1. Nominal dimensions and structure of the analyzed plates.

The infill of the face layers and the perimeter frame was set to 100% for all specimens. The plates were printed in a horizontal orientation, with their largest surfaces parallel to the build platform. The bottom and top face sheets consisted of seven and four printed layers, respectively, with alternating raster orientations of +45° and −45° relative to the principal axes of the plate. The unequal number of layers in the bottom and top outer layers resulted in a slightly asymmetrical configuration throughout the entire thickness of the panel. This configuration was intentionally chosen to demonstrate the applicability of the proposed identification methodology in determining the equivalent material properties of plates that deviate from the usual symmetric structure. The internal lattice core was generated using the regular infill pattern (Pattern 0) available in the slicing software. Other basic geometric parameters of the plates, particularly the thickness of the bottom and top face layers, the width of the perimeter frame, and the height of the core, remained constant for all analyzed

specimens. Thus, the nominal core infill density was the only systematically varied printing parameter affecting the internal core geometry.

For the purposes of this study, one plate specimen was fabricated and experimentally tested for each of the investigated core infill densities. The masses of individual specimens determined by weighing are listed in Table 2. The measured mass is included directly in the process of identifying equivalent material properties, together with the external dimensions of the specimen, to calculate the equivalent density of the homogenized plate.

Table 2. Mass of the analyzed plates as a function of core infill density.

Core infill	20%	40%	60%	80%	100%
Mass [g]	30.5	36.6	42.7	48.8	61.6

2.2. Experimental Modal Analysis

The natural frequencies and mode shapes of the plates represent additional key input data for the identification of equivalent material constants. For this reason, all investigated plates were subjected to experimental modal analysis (EMA) performed under quasi-free boundary conditions.

The vibration response was measured using a Polytec PDV-100 (Polytec GmbH, Waldbronn, Germany) single-point laser Doppler vibrometer, which remained stationary during the measurement and recorded the vibration velocity as normal to the plate surface at a suitably selected reference point. An ultraminiature Dytran 5800SL (Dytran Instruments, Inc., Chatsworth, CA, USA) impulse hammer was used to excite the structure. The measurements were performed using the roving-hammer method, with each plate sequentially excited at 40 points defined on its upper surface. This arrangement, while maintaining a fixed vibrometer position, enabled the construction of a set of frequency response functions (FRFs) required for the identification of the natural frequencies and corresponding mode shapes. The frequency evaluated during the measurements was 0–2500 Hz, which enabled the identification of at least the first 10 flexible modes for each analyzed plate.

During the measurement, the plate was suspended horizontally on two elastic cords, as shown in Figure 2, to approximate free–free boundary conditions. The stiffness of the elastic cords was selected in such a way that the highest natural frequency associated with the rigid-body modes of the specimen did not exceed 10% of the lowest natural frequency corresponding to its first flexible mode. Therefore, the influence of the compliant suspension on the modal characteristics of the plate itself was minimized.

The measurements and signal processing were performed using the PULSE system with the DAQ module LAN-XI Type 3050 (Brüel & Kjær Sound & Vibration Measurement A/S, Nærum, Denmark). The sampling frequency was set to 6400 Hz, with a time record length of 0.32 s, corresponding to a frequency resolution of 3.125 Hz. For each investigated plate, the measurements were repeated three times at each degree of freedom, and the resulting frequency response functions (FRFs) were obtained by averaging. The modal parameters were subsequently identified from the FRF matrix using the Rational Fraction Polynomial-Z (RFP-Z) method. The experimental modal analysis resulted in a set of natural frequencies and their corresponding mode shape vectors obtained for each investigated plate. These experimentally identified modal parameters subsequently served as reference data for the optimization-based identification of the equivalent material properties of the homogenized plates.

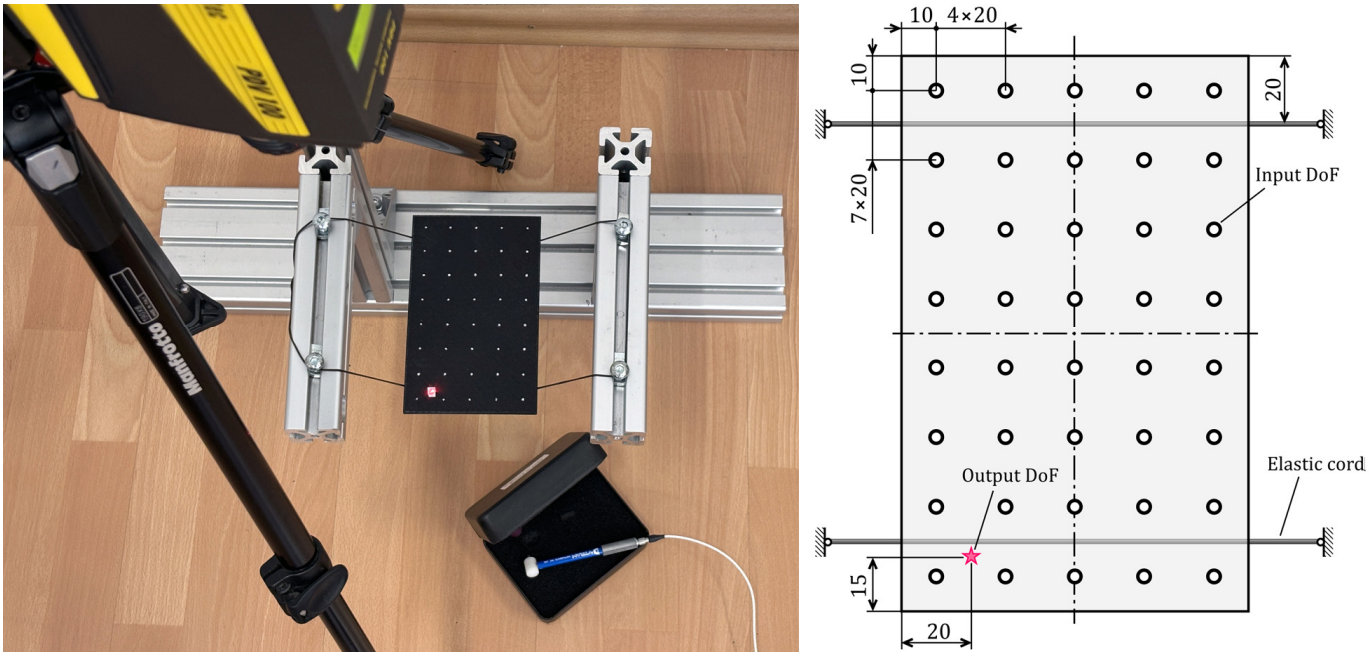

Figure 2. Experimental setup for modal parameters identification and schematic representation of the excitation points (Input DoF), response measurement point (Output DoF), and elastic suspension locations.

2.3. Homogenized Plate Model and Ritz Solution

The objective of homogenization is to replace the 3D-printed heterogeneous plate with a lattice core by an equivalent homogeneous plate that has the same mass and the same overall dimensions. Based on these parameters, the equivalent density of the homogenized plate is first calculated as

$$\rho = \frac{m}{V} = \frac{m}{abh}, \tag{1}$$

where m is the measured mass of the printed plate, a is the plate length, b is the plate width, and h is the total plate thickness. Since the equivalent density ρ was calculated independently of the nominal core infill density specified in the slicing software, it is worth emphasizing that the core infill density does not enter the formulation of the mass or stiffness matrices within the computational framework described later in this section.

Although the square lattice structure exhibits symmetry resulting in identical effective elastic behavior in the x and y directions, its response to shear loading does not necessarily satisfy the conditions of isotropy. The effective shear deformation of the lattice results from a combination of tensile and compressive deformation, bending, and rotation of the individual ribs and their joints. Therefore, instead of an isotropic model, an orthotropic constitutive model with square symmetry [29] is used to describe the elastic behavior of the homogenized plate. This model is characterized by three independent equivalent elastic constants:

$$E = E_x = E_y, \quad \nu = \nu_{xy} = \nu_{yx}, \quad G = G_{xy}. \tag{2}$$

Unlike the isotropic model, the shear modulus G is not constrained by the relation $G = \frac{E}{2(1+\nu)}$, but it is identified as an independent material parameter. This allows the homogenized model to independently capture the effective shear response of the lattice structure and the associated torsional stiffness of the plate. The introduction of an independent shear modulus is particularly important for reproducing natural frequencies and mode shapes with a pronounced torsional component, whose dynamic response is sensitive to the value of the coefficient D_{66}. The bending stiffness coefficients of the homogenized plate used

in the subsequent solution of the modal problem by the Ritz method are defined for the constitutive model as follows [30,31]:

$$D_{11} = \frac{Eh^3}{12(1-\nu^2)}, \tag{3}$$

$$D_{22} = D_{11}, \tag{4}$$

$$D_{12} = \nu D_{11}, \tag{5}$$

$$D_{66} = \frac{Gh^3}{12}, \tag{6}$$

where the coefficients D_{11} and D_{22} represent the bending stiffnesses in the principal directions of the plate; D_{12} characterizes a coupling between the curvatures in these directions; and D_{66} represents a twisting stiffness. It should be emphasized that, in the adopted orthotropic model with square symmetry, the coefficient D_{66} is not constrained by the other bending stiffness coefficients, i.e., in general, the relation $D_{66} = \frac{1}{2}(D_{11} - D_{12})$, which is characteristic for an isotropic material model, does not apply. As shown later, this approach contributes to improved agreement between the numerically predicted and experimentally identified modes.

The natural frequencies and mode shapes of the free homogenized plate are determined using the Ritz method [32,33], in which the transverse displacement $w(x, y, t)$ of the plate mid-surface is approximated by a finite sum of suitable basis functions, i.e.,

$$w(x,y,t) = \sum_{p=1}^{N_p} q_p(t)\phi_p(x,y), \tag{7}$$

where ϕ_p represents the selected spatial basis functions and q_p represents the corresponding generalized coordinates. Introducing dimensionless coordinates,

$$\xi = \frac{x}{a}, \quad \eta = \frac{y}{b}, \quad 0 \le \xi \le 1, \quad 0 \le \eta \le 1, \tag{8}$$

the transverse displacement given by Equation (7) can be expressed using a tensor product expansion of shifted orthonormal Legendre polynomials

$$w(\xi,\eta,t) = \sum_{i=0}^{N_x-1}\sum_{j=0}^{N_y-1} q_{ij}(t)\hat{P}_i(\xi)\hat{P}_j(\eta), \tag{9}$$

where q_{ij} represents the generalized coordinates, and N_x and N_y denote the numbers of Legendre polynomial basis functions in the x and y directions, respectively. The corresponding polynomial degrees range from 0 to $N_x - 1$ and $N_y - 1$, giving the total number of generalized coordinates:

$$N_p = N_x N_y. \tag{10}$$

The shifted orthonormal Legendre polynomials are defined as follows [34]:

$$\hat{P}_n(z) = \sqrt{2n+1}P_n(2z-1), \quad z = \begin{cases}\xi \\ \eta\end{cases}, \tag{11}$$

where P_n is the standard Legendre polynomial of degree n. The functions given by Equation (11) satisfy the orthonormality condition over the interval ⟨0,1⟩:

$$\int_0^1 \hat{P}_i(z)\hat{P}_j(z)\mathrm{d}z = \delta_{ij}, \tag{12}$$

where δ_{ij} is the Kronecker delta.

For a thin Kirchhoff-type plate, the kinetic energy T and the bending strain energy U can be expressed as follows [35]:

$$T = \frac{1}{2}\rho h \int_0^a \int_0^b \left(\frac{\partial w}{\partial t}\right)^2 \mathrm{d}y\mathrm{d}x, \tag{13}$$

$$U = \frac{1}{2}\int_0^a \int_0^b \left[D_{11}\left(\frac{\partial^2 w}{\partial x^2}\right)^2 + 2D_{12}\frac{\partial^2 w}{\partial x^2}\frac{\partial^2 w}{\partial y^2} + D_{22}\left(\frac{\partial^2 w}{\partial y^2}\right)^2 + 4D_{66}\left(\frac{\partial^2 w}{\partial x \partial y}\right)^2\right]\mathrm{d}y\mathrm{d}x, \tag{14}$$

where the second partial derivatives of the transverse displacement function with respect to x and y represent the curvatures associated with the bending and torsional deformation of the plate.

Substituting the Ritz approximation (9) into Equations (13) and (14) yields the standard discrete expressions for the kinetic and strain energies:

$$T = \frac{1}{2}\,\dot{\mathbf{q}}^T \mathbf{M}\dot{\mathbf{q}}, \tag{15}$$

$$U = \frac{1}{2}\mathbf{q}^T \mathbf{K}\mathbf{q}, \tag{16}$$

where $\mathbf{M}$ and $\mathbf{K}$ represent the mass and stiffness matrices of the homogenized plate model, respectively, while $\mathbf{q}$ and $\dot{\mathbf{q}}$ are the vectors of generalized coordinates and generalized velocities.

The two polynomial basis functions expressed in terms of the dimensionless coordinates (8) are defined as

$$\phi_{ij}(\xi, \eta) = \hat{P}_i(\xi)\hat{P}_j(\eta). \tag{17}$$

Owing to the orthonormality of the selected basis given by Equation (12), the corresponding element of the mass matrix can be simplified to

$$M_{ij,kl} = \rho abh \int_0^1 \int_0^1 \phi_{ij}(\xi, \eta)\phi_{kl}(\xi, \eta)\,\mathrm{d}\xi\mathrm{d}\eta = \rho abh\,\delta_{ik}\delta_{jl}, \tag{18}$$

resulting in a diagonal mass matrix:

$$\mathbf{M} = \rho abh\mathbf{I}, \tag{19}$$

where $\mathbf{I}$ is the identity matrix. Excluding the off-diagonal mass coupling between generalized coordinates simplifies the numerical solution of the eigenvalue problem.

The stiffness matrix is assembled from the bending and twisting contributions of Equation (14). Using the separable structure of the Legendre basis, it can be expressed as

$$\begin{aligned}\mathbf{K} = ab\Big[&\tfrac{D_{11}}{a^4}\left(\mathbf{G}_x^{(2,2)} \otimes \mathbf{G}_y^{(0,0)}\right) + \tfrac{D_{22}}{b^4}\left(\mathbf{G}_x^{(0,0)} \otimes \mathbf{G}_y^{(2,2)}\right) \\ &+ \tfrac{D_{12}}{a^2b^2}\left(\mathbf{G}_x^{(2,0)} \otimes \mathbf{G}_y^{(0,2)} + \mathbf{G}_x^{(0,2)} \otimes \mathbf{G}_y^{(2,0)}\right) + \tfrac{4D_{66}}{a^2b^2}\left(\mathbf{G}_x^{(1,1)} \otimes \mathbf{G}_y^{(1,1)}\right)\Big],\end{aligned} \tag{20}$$

where $\otimes$ denotes the Kronecker product and $\mathbf{G}_x^{(r,s)}$ and $\mathbf{G}_y^{(r,s)}$ are one-dimensional derivative Gram matrices. Their elements are evaluated using the Gauss–Legendre quadrature [34]:

$$G_{ij}^{(r,s)} = \int_0^1 \hat{P}_i^{(r)}(z)\hat{P}_j^{(s)}(z)\mathrm{d}z \approx \sum_{p=1}^{N_q} w_p \hat{P}_i^{(r)}\left(z_p\right)\hat{P}_j^{(s)}\left(z_p\right), \tag{21}$$

where $r, s \in \{0,1,2\}$ denote derivative orders, and z_p and w_p are the quadrature points and weights on the interval $\langle 0,1\rangle$. The number of quadrature points is selected as $N_q = \max(N_p + 2, 4)$, where N_p is the number of Legendre basis functions in the corresponding coordinate direction. Since the integrands are polynomials, the selected quadrature order provides exact integration in exact arithmetic. This approach enables efficient assembly of the stiffness matrix without direct two-dimensional numerical integration.

After assembling the mass and stiffness matrices, the natural frequencies and mode shapes of the homogenized plate are determined by solving the generalized eigenvalue problem

$$\mathbf{K}\mathbf{q}_r = \omega_r^2 \mathbf{M}\mathbf{q}_r, \tag{22}$$

where ω_r is the r-th natural angular frequency and $\mathbf{q}_r$ is the corresponding eigenvector containing the Ritz coefficients. The mode shape of the r-th mode is obtained by substituting these coefficients into Equation (9). The corresponding natural frequency in Hz is then determined using the well-known relation $f_r = \frac{\omega_r}{2\pi}$.

Since the plate is considered with free–free boundary conditions, the solution also contains three rigid-body modes with zero natural frequencies. These modes are excluded from further processing, and only the first N flexible modes are used for the subsequent identification of the equivalent material parameters.

The similarity between the experimental (reference) and calculated mode shape vectors is quantified using the Cross-Modal Assurance Criterion (Cross-MAC) [36]

$$MAC_{rs} = \frac{\left(\boldsymbol{\Psi}_r^T \boldsymbol{\Psi}_s\right)^2}{\left(\boldsymbol{\Psi}_r^T \boldsymbol{\Psi}_r\right)\left(\boldsymbol{\Psi}_s^T \boldsymbol{\Psi}_s\right)}, \tag{23}$$

where $\boldsymbol{\Psi}_r$ represents the vector of the r-th reference mode shape and $\boldsymbol{\Psi}_s$ represents the vector of the s-th numerically predicted mode shape. The correlation of all combinations of mode shapes results in a MAC matrix, whose elements take values ranging from 0 to 1. The criterion is independent of vector scaling. A value approaching 1 indicates a high degree of agreement between the compared mode shapes, whereas a value close to zero indicates low similarity.

During the identification process, the complete $N \times N$ MAC matrix is evaluated. However, only its MAC_{rr} diagonal elements, quantifying the agreement between the mutually paired experimental and numerically predicted flexible mode shapes, are used in the formulation of the optimization objective function. For correct mode pairing and good agreement between the modal models, high values (ideally close to 1) are therefore expected along the main diagonal of the MAC matrix, while the off-diagonal elements are expected to approach zero. This approach significantly reduces the computational time required for the identification of the unknown material parameters.

2.4. Identification of Equivalent Material Properties

The equivalent elastic constants E, ν and G of the homogenized plates are identified simultaneously. Considering the differences in their orders of magnitude, normalized design variables x_1, x_2 and x_3 are introduced into the optimization problem to improve the numerical conditioning of the objective function. At each iteration of the optimization procedure, these variables are scaled by the initial values of the parameters to be identified, as follows:

$$E_k = x_1 E_0, \quad \nu_k = x_2 \nu_0, \quad G_k = x_3 G_0, \tag{24}$$

where E_0 and ν_0 correspond to the material properties of the base material (Table 1) used to manufacture the plates, while the initial value of the shear modulus G_0 is determined using the relation

$$G_0 = \frac{E_0}{2(1+\nu_0)}, \tag{25}$$

which is valid for an isotropic material. It should be emphasized that Equation (25) is used only to determine the initial value of G. During the subsequent identification procedure, G is optimized independently of E and ν.

The optimization is initialized using a normalized design vector

$$\mathbf{x}_{k=0} = \begin{bmatrix} x_{10} & x_{20} & x_{30} \end{bmatrix}^T, \tag{26}$$

where $x_{i0} \in \langle 0,1 \rangle$ for $i = 1,2,3$. The selection of initial parameter estimates is discussed in more detail in Section 2.6.

For each trial parameter vector $\mathbf{x}_k$, the bending stiffness coefficients are recalculated according to Equations (3)–(6); the Ritz eigenvalue problem is solved; and the natural frequencies and mode shapes of the first N flexible modes are compared with their experimentally identified counterparts. The relative deviation of the r-th natural frequency is defined as

$$e_r^f = \frac{f_{r,calc} - f_{r,ref}}{f_{r,ref}}, \tag{27}$$

where $f_{r,calc}$ is the calculated natural frequency and $f_{r,ref}$ is the experimentally identified target natural frequency.

The corresponding mode shape deviation is defined using the diagonal element of the MAC matrix as follows:

$$e_r^{MAC} = 1 - MAC_{rr}. \tag{28}$$

The combined scalar objective function is then expressed as

$$J(\mathbf{x}) = w_f \sum_{r=1}^{N} \left(e_r^f\right)^2 + w_m \sum_{r=1}^{N} \left(e_r^{MAC}\right)^2, \tag{29}$$

where w_f and w_m are weighting coefficients, controlling the contributions of the natural frequency and mode shape agreement, respectively. The values of the weighting coefficients can be selected independently according to the desired relative importance of the individual components of the objective function. The influence of these coefficients on the identification results is systematically evaluated through the sensitivity analysis presented in Section 2.6.

The equivalent material parameters are identified using a suitable optimization method. The optimization problem is formulated as

$$\mathbf{x}^* = \arg\min_{\mathbf{x}} J(\mathbf{x}). \tag{30}$$

The resulting equivalent material parameters are then determined as

$$E^* = x_1^* E_0, \quad \nu^* = x_2^* \nu_0, \quad G^* = x_3^* G_0. \tag{31}$$

The identified parameters are subsequently substituted into Equations (3)–(6) to calculate the equivalent bending stiffness coefficients.

2.5. Computational Workflow of the Identification Algorithm

The methodology for identifying the equivalent material parameters described in the previous sections was implemented and tested in MATLAB R2025b (The MathWorks, Inc., Natick, MA, USA). The developed program employs an iterative optimization algorithm, combining the forward calculation of the modal parameters of the homogenized plate model with their comparison against the experimentally identified reference data at each iteration. The MATLAB code (equivalent_properties_identification.m) is available as Supplementary Material accompanying this article.

Based on the selected core infill density, the program loads the corresponding MAT-file containing the reference data for the analyzed plate. These data include the experimentally identified natural frequencies $\{f_{ref}\}$, the corresponding mode shapes, the plate mass m, and its measured dimensions a, b and h. The equivalent density ρ of the homogenized plate is subsequently calculated according to Equation (1). The experimental mode shapes were

obtained at 40 uniformly distributed measurement points forming an 8 × 5 grid on the plate surface. The mode shapes were transformed into real-valued modal vectors through phase normalization and suppression of their imaginary components and subsequently exported from PULSE Reflex 21.0 software (Brüel & Kjær Sound & Vibration Measurement A/S, Nærum, Denmark) as matrices of normal vibration amplitudes. Prior to their use in the identification procedure, the experimental mode shapes were spatially extrapolated in MATLAB using a linear approximation to account for the offset of the measurement points from the plate edges. The original 8 × 5 amplitude matrices were thus mapped onto an equally sized grid extending to the plate edges, which is consistent with the spatial discretization in the Ritz-based computational model. This ensures spatial correspondence between the calculated and reference mode shapes when evaluating the MAC. The reference modal data are stored in the MAT file as a three-dimensional matrix $[V_{ref}]$, with its r-th layer representing the spatial distribution of the amplitudes of the r-th reference mode shape. The individual mode shapes are arranged in advance so that their order corresponds to the order of the natural frequencies stored in the vector $\{f_{ref}\}$. The first N flexible modes are then selected from the available reference dataset and used in the optimization procedure. In this study, eight modes were used to identify the equivalent material properties.

The objective of the optimization algorithm is to minimize the objective function defined in Equation (29). For this purpose, the MATLAB function fminsearch, based on the derivative-free Nelder–Mead simplex method [37], was used.

At each iteration, the optimizer updates the equivalent material parameters E, ν and G. Based on these updated parameters, the modal problem of the homogenized plate is solved using the Ritz method, and the resulting predicted modal parameters are compared with the reference data. The iterative process continues until the specified convergence criteria are satisfied.

Upon convergence, the optimization algorithm returns the identified equivalent material constants together with the equivalent density, and the program subsequently calculates the corresponding bending stiffness coefficients D_{11}, D_{22}, D_{12} and D_{66} of the homogenized plate. The output also includes the predicted natural frequencies, their percentage deviations from the reference values, and the diagonal elements of the resulting MAC matrix. For a more detailed assessment of the identified model, the reference and predicted mode shapes are displayed together with their corresponding natural frequencies, and the complete MAC matrix is visualized separately. The overall computational procedure, including the input of experimental data, iterative identification of the equivalent material properties, Ritz-based modal analysis, modal correlation, and evaluation of the optimization objective function, is summarized in the flowchart shown in Figure 3.

2.6. Sensitivity Analysis

Preliminary calculations indicated that the identification results are sensitive to the settings of the computational model and optimization procedure. Therefore, a sensitivity analysis was performed to assess the influence of the Legendre polynomial basis size, the objective-function weighting coefficients, and the initial parameter estimates on the identification results.

The transverse displacement field of the plate is approximated using a Legendre polynomial basis of dimensions $N_x \times N_y$. The basis dimensions determine the number of approximation terms and thus influence the accuracy of the predicted natural frequencies and numerical mode shapes. Therefore, the effect of the basis size was investigated first, assuming $N_x = N_y$. Eight basis configurations were considered: 5 × 5, 6 × 6, 8 × 8, 10 × 10, 12 × 12, 16 × 16, 20 × 20, and 24 × 24. For this analysis, the objective-function weighting coefficients were fixed at $w_f = w_m = 1$, and the normalized initial parameter vector was set to

$\mathbf{x}_0 = [1\ 1\ 1]^T$. The sensitivity was evaluated in terms of the mean deviations between the predicted and experimental modal parameters and the relative changes in the identified elastic constants with respect to the 24 × 24 basis, which was adopted as the reference solution.

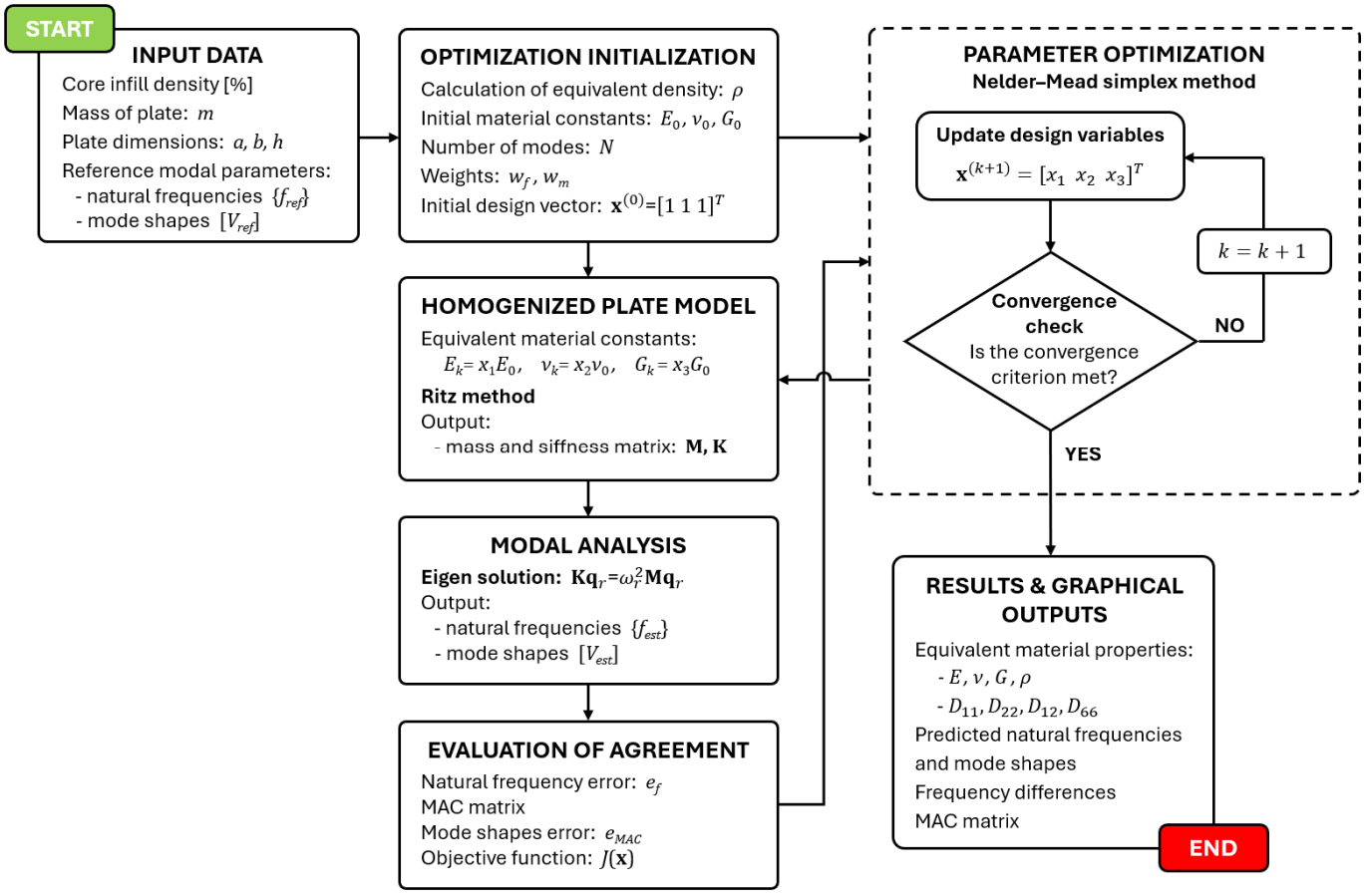

Figure 3. Schematic flowchart of the computational algorithm.

Table 3 summarizes the influence of the basis size on the identification results for all five investigated plates. The evaluation criteria include the mean absolute relative deviation between the calculated and experimental natural frequencies ($\overline{\Delta f}$), the mean value of the diagonal elements of the MAC matrices ($\overline{MAC}$), and the mean absolute relative differences in the identified elastic constants $\left(\overline{\Delta E}, \overline{\Delta \nu}, \overline{\Delta G}\right)$ with respect to the 24 × 24 reference solution. The frequency and mode-shape discrepancies were averaged over eight identified modes and five plates, whereas the relative differences in the elastic constants were calculated separately for each plate and subsequently averaged.

As Table 3 shows, the 5 × 5 basis exhibited insufficient approximation accuracy. Increasing the basis size to 6 × 6 substantially improved the agreement between the calculated and experimental modal parameters. However, the identified elastic constants continued to vary with increasing basis size, indicating that the smaller bases had not yet provided sufficiently converged identification results. From the 12 × 12 basis onwards, the identified elastic constants showed substantially reduced sensitivity to further increases in the basis size. Compared with the 24 × 24 reference solution, the mean absolute relative differences in Young's modulus, Poisson's ratio, and shear modulus were only 0.189%, 0.161%, and 0.246%, respectively, for the 12 × 12 basis. Further increasing the basis size reduced all three differences to below 0.01%, indicating near-complete convergence of the identified material parameters, albeit at the expense of increased computational cost.

Based on these results, the 12 × 12 Legendre basis was selected for the subsequent identification calculations, as further increases in the basis size resulted in only marginal changes in the natural frequency deviations and mode shape agreement, while the identified elastic constants were already sufficiently converged. This basis size therefore provides a reasonable compromise between identification accuracy, numerical convergence, and computational efficiency.

Table 3. Sensitivity of the identification results to the dimensions of the Legendre–Ritz polynomial basis ($w_f = w_m = 1$, $\mathbf{x}_0 = [1\ 1\ 1]^T$).

$N_x = N_y$	$\overline{\Delta f}$ [%]	$\overline{MAC}$ [–]	$\overline{\Delta E}$ [%]	$\overline{\Delta \nu}$ [%]	$\overline{\Delta G}$ [%]
5	9.484	0.7018	37.83	23.34	16.75
6	1.483	0.9466	3.243	5.967	1.590
8	1.387	0.9457	3.431	9.728	2.868
10	1.790	0.9442	0.705	3.649	0.539
12	1.715	0.9448	0.189	0.161	0.246
16	1.727	0.9448	0.008	0.001	0.008
20	1.727	0.9448	0.008	0.001	0.008
24	1.728	0.9448	0.000	0.000	0.000

Subsequently, the sensitivity of the identification results to the objective function weighting coefficients and initial parameter estimates was investigated. The aim was to determine a suitable combination of these settings that provides a favorable balance between the accuracy of the predicted modal parameters and the consistency of the identified equivalent elastic constants across the investigated plates. Three normalized initial design vectors, $\mathbf{x}_0 = [0.1\ 0.1\ 0.1]^T$, $\mathbf{x}_0 = [0.5\ 0.5\ 0.5]^T$, and $\mathbf{x}_0 = [1\ 1\ 1]^T$, were considered, while the mode-shape weighting coefficient w_m was varied over the values 0, 0.05, 0.1, 0.5, 1, 2, 3, 4, and 5. The frequency weighting coefficient was fixed at $w_f = 1$, and the Legendre basis size was maintained at 12 × 12, as established by the preceding sensitivity analysis.

For each combination of w_m and $\mathbf{x}_0$, the equivalent elastic constants were identified for all five investigated plates. The agreement between the calculated and experimental modal parameters was evaluated using the mean absolute relative frequency deviation ($\overline{\Delta f}$) and the mean value of the diagonal elements of the MAC matrices ($\overline{MAC}$). As in the preceding sensitivity analysis, both indicators were obtained by averaging the corresponding values over all five plates and the first eight flexible modes, considering only the diagonal elements of the MAC matrices. The resulting values for all investigated parameter combinations are summarized in Table 4.

Table 4. Sensitivity of the identification results to the mode-shape weighting coefficient and initial parameter estimates.

	$\mathbf{x}_0 = [0.1\ 0.1\ 0.1]^T$		$\mathbf{x}_0 = [0.5\ 0.5\ 0.5]^T$		$\mathbf{x}_0 = [1.0\ 1.0\ 1.0]^T$	
w_m	$\overline{\Delta f}$ [%]	$\overline{MAC}$ [–]	$\overline{\Delta f}$ [%]	$\overline{MAC}$ [–]	$\overline{\Delta f}$ [%]	$\overline{MAC}$ [–]
0	1.1287	0.7998	1.1906	0.8445	0.6983	0.8887
0.05	0.8535	0.8921	0.8535	0.8921	0.9315	0.9389
0.1	0.9672	0.8934	0.9672	0.8934	1.0435	0.9402
0.5	0.7711	0.8907	1.1181	0.8948	1.9066	0.9385
1	1.3796	0.8967	1.3796	0.8967	1.4544	0.9435
2	1.6502	0.8980	1.6502	0.8980	1.7151	0.9448
3	1.9860	0.8991	2.0900	0.8979	3.1645	0.9449
4	2.2091	0.8997	2.2091	0.8997	2.3403	0.9458
5	2.3942	0.9001	2.3665	0.9000	2.4966	0.9461

The results presented in Table 4 indicate that both the mode-shape weighting coefficient w_m and the initial parameter estimates $\mathbf{x}_0$ influence the identification results. The initial vectors $\mathbf{x}_0 = [0.1\ 0.1\ 0.1]^T$ and $\mathbf{x}_0 = [0.5\ 0.5\ 0.5]^T$ generally yielded slightly lower mean frequency deviations but noticeably lower mean MAC values compared with $\mathbf{x}_0 = [1\ 1\ 1]^T$. The reduced mode-shape correlation was primarily associated with incorrect pairing of modes with closely spaced natural frequencies. Increasing w_m generally improved the mean MAC value, although this improvement was accompanied by increasing frequency deviations. For $\mathbf{x}_0 = [1\ 1\ 1]^T$, the $\overline{MAC}$ increased only marginally beyond $w_m = 0.05$, whereas $\overline{\Delta f}$ increased more substantially. Therefore, $w_m = 0.05$ and $\mathbf{x}_0 = [1\ 1\ 1]^T$ were selected for the subsequent identification calculations, providing a favorable compromise between the agreement of calculated and experimental natural frequencies and mode shapes.

3. Results

3.1. Modal Parameters of 3D-Printed Plates

For each of the analyzed plates, ten flexible modes were identified by experimental modal analysis. Their natural frequencies f_r, which were subsequently used as reference values in the identification of the equivalent material properties, together with the corresponding damping ratios ζ_r, are listed in Table 5.

Table 5. Natural frequencies and damping ratios of the analyzed plates determined by experimental modal analysis.

	20%		**40%**		**60%**		**80%**		**100%**	
Mode r	f_r **[Hz]**	ζ_r **[%]**	f_r **[Hz]**	ζ_r **[%]**	f_r **[Hz]**	ζ_r **[%]**	f_r **[Hz]**	ζ_r **[%]**	f_r **[Hz]**	ζ_r **[%]**
1	210.84	1.27	207.86	1.22	205.33	1.33	209.53	1.73	223.86	1.26
2	216.03	1.30	242.22	1.37	237.63	1.39	233.72	1.63	230.32	1.06
3	468.74	1.29	535.49	0.84	526.85	0.90	521.52	1.06	522.45	0.91
4	566.31	0.69	556.86	0.86	556.83	0.93	568.74	0.77	606.46	1.49
5	574.01	0.45	613.40	0.57	575.46	0.64	582.19	1.06	620.39	0.86
6	719.46	0.87	758.63	0.88	757.43	0.88	762.65	0.93	793.68	0.91
7	855.79	0.84	941.98	0.76	933.85	0.81	931.69	0.97	952.13	0.85
8	1026.8	0.63	1109.4	0.77	1108.2	0.72	1111.8	0.73	1128.9	0.69
9	1199.2	0.74	1195.7	0.71	1260.8	0.48	1228.1	0.71	1298.9	0.65
10	1406.6	0.78	1422.6	0.74	1430.6	0.85	1451.7	0.81	1525.4	0.67

For illustration, Figure 4 shows the first nine flexible mode shapes of the plate with a 40% core infill density, obtained by experimental modal analysis in PULSE Reflex 21.0 and subsequently imported into MATLAB R2025b. In addition to the mode number, each mode shape is classified according to the nodal-line convention using the notation (m, n), where m and n denote the numbers of nodal lines intersecting the x- and y-axes, respectively.

The ordering of the mode shapes shown in Figure 4 was identical for the plates with core infill densities of 40%, 60%, 80%, and 100%. In contrast, a different ordering was observed for the plate with a 20% core infill density, with the first and second mode shapes, as well as the fourth and fifth mode shapes, being interchanged compared to the other plates. Both mode pairs are characterized by closely spaced natural frequencies, as can be seen in Table 5. The ordering of flexible modes identified for all analyzed plates is summarized in Table 6, where the modes are arranged in ascending order of natural frequency.

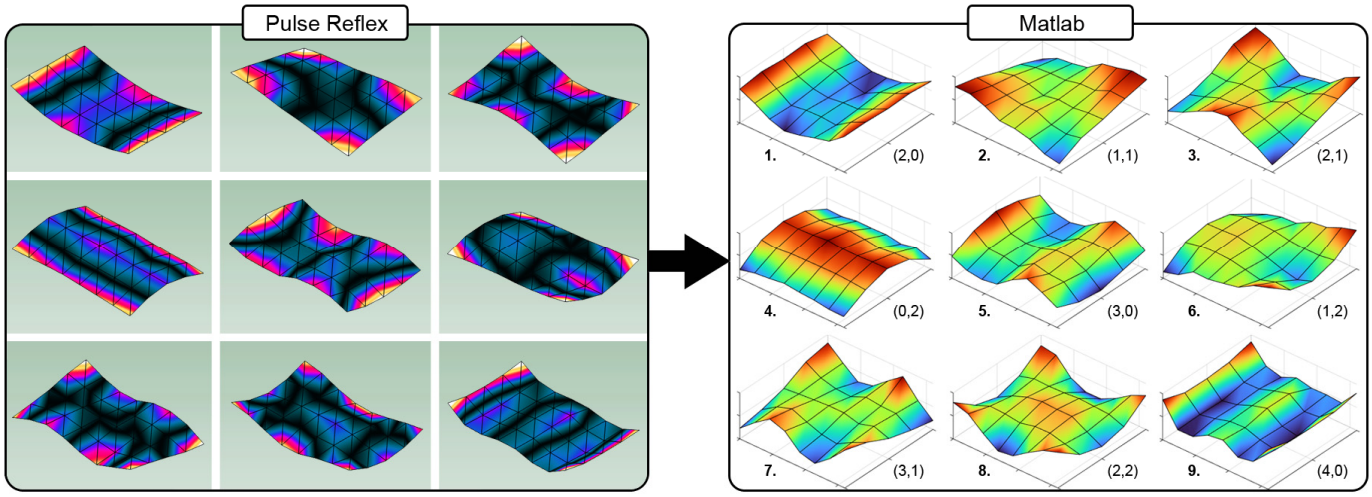

Figure 4. Experimental mode shapes of the plate with 40% core infill transferred from PULSE Reflex to MATLAB and classified according to the nodal-line convention.

Table 6. Order and nodal-line classification of the flexible vibration modes of the analyzed plates.

	Mode r (m, n)									
Core Infill [%]	**1**	**2**	**3**	**4**	**5**	**6**	**7**	**8**	**9**	**10**
20	(2,0)	(1,1)	(2,1)	(0,2)	(3,0)	(1,2)	(3,1)	(2,2)	(4,0)	(4,2)
40, 60, 80, 100	(1,1)	(2,0)	(2,1)	(3,0)	(0,2)	(1,2)	(3,1)	(2,2)	(4,0)	(4,2)

3.2. Identified Equivalent Material Properties and Model Validation

Table 7 summarizes the identified equivalent material properties and the corresponding bending stiffness coefficients derived for the homogenized models of all analyzed plates. The plate with a 100% core infill density was also included in the identification procedure. Even at full infill, perfectly homogeneous and isotropic behavior cannot be automatically assumed due to the layered nature of additive manufacturing and the orientation of the extruded material paths.

Table 7. Identified equivalent material properties and bending stiffness coefficients of the analyzed plates ($w_f = 1$, $w_m = 0.05$).

Core Infill	ρ [kg/m³]	E [MPa]	ν [–]	G [MPa]	$D_{11} = D_{22}$ [Nm]	D_{12} [Nm]	D_{66} [Nm]	$\overline{\Delta f}$ [%]	$\overline{MAC}$ [–]
20%	476.6	796.1	0.414	294.4	5.124	2.121	1.57	1.57	0.919
40%	571.9	1005	0.296	487.6	5.872	1.736	2.6	1.67	0.927
60%	667.0	1099	0.388	547.7	6.897	2.675	2.921	0.76	0.929
80%	762.3	1283	0.398	614.9	8.127	3.231	3.279	0.28	0.954
100%	962.5	1855	0.384	751.0	11.608	4.461	4.005	0.39	0.966

The first eight flexible modes were included in the identification procedure. This number provided a sufficient set of modal information for the simultaneous identification of all three unknown elastic constants. The identification was performed using a 12 × 12 Legendre polynomial basis, objective-function weighting coefficients of $w_f = 1$ and $w_m = 0.05$, and an initial design vector of $\mathbf{x}_0 = [1\ 1\ 1]^T$. The agreement between the calculated and experimental modal parameters is quantified in Table 7 using the mean absolute relative frequency deviation, $\overline{\Delta f}$, and the mean value of the diagonal elements of the MAC matrix, $\overline{MAC}$.

The identified equivalent material constants exhibit a clear trend with respect to the core infill density. As the core infill density decreases, both Young's modulus E and shear

modulus G decrease, accompanied by a corresponding reduction in the bending stiffness coefficients D_{11}, D_{22}, D_{12} and D_{66}. Poisson's ratio ν, however, exhibits a different trend, varying non-monotonically between 0.296 and 0.414 without a clear dependence on the core infill density. Its lowest value is obtained for the plate with 40% infill, while the highest corresponds to the plate with 20% infill. At 100% infill, Poisson's ratio reaches 0.384, indicating that its variation cannot be directly associated with the transition from a lattice-core configuration to a fully filled plate structure.

The identified parameters also provide good agreement between the predicted modal parameters and the experimental results. The mean absolute relative deviation of the natural frequencies, $\overline{\Delta f}$, ranges from 0.28% to 1.67%, with the lowest value obtained for the plate with 80% core infill density and the highest for the plate with 40% core infill density. The mean value of the diagonal MAC elements, $\overline{MAC}$, ranges from 0.919 for the plate with 20% core infill density to 0.966 for the plate with 100% core infill density, indicating a high degree of agreement between the experimental and predicted mode shapes. The values obtained for both criteria confirm that the homogenized models reproduce the experimentally determined modal characteristics with good accuracy.

As shown in Table 8, the absolute relative deviations of the individual predicted natural frequencies do not exceed 3.6%, with the largest discrepancies occurring predominantly for plates with lower core infill densities.

Table 8. Predicted natural frequencies of homogenized plate models and their relative deviations from reference values for plates with different core infill densities.

	20%		**40%**		**60%**		**80%**		**100%**	
Mode r	f_r **[Hz]**	Δf **[%]**	f_r **[Hz]**	Δf **[%]**	f_r **[Hz]**	Δf **[%]**	f_r **[Hz]**	Δf **[%]**	f_r **[Hz]**	Δf **[%]**
1	204.87	–2.83	213.92	+2.92	207.85	+1.23	210.17	+0.30	224.68	+0.37
2	209.27	–3.13	238.13	–1.69	234.12	–1.48	232.37	–0.58	229.58	–0.32
3	471.21	+0.53	530.59	–0.92	522.86	–0.76	521.02	–0.10	522.5	+0.01
4	571.4	+0.90	565.12	+1.48	562.72	+1.06	570.76	+0.36	607.65	+0.20
5	571.4	–0.46	591.37	–3.59	576.38	+0.16	581.85	–0.06	616.87	–0.57
6	735.55	+2.24	753.89	–0.63	754.73	–0.36	760.79	–0.24	790.08	–0.45
7	866.97	+1.31	942.37	+0.04	929.46	–0.47	930.45	–0.13	950.07	–0.22
8	1039.0	+1.19	1132.3	+2.06	1114.4	+0.56	1116.7	+0.44	1139.8	+0.97
$\overline{\Delta f}$		1.57		1.67		0.76		0.28		0.39

The diagonal elements of the MAC matrices reported in Table 9 range from 0.822 to 0.984. The lowest agreement was observed for the sixth mode of the plate with 20% core infill density and the eighth mode of the plate with 60% core infill density, both exhibiting an MAC value of 0.822. Nevertheless, the MAC values exceed 0.9 for most of the remaining modes, indicating good agreement between the reference and predicted mode shapes. Furthermore, a consistent improvement in the mean mode shape agreement can be observed with increasing core infill density, with $\overline{MAC}$ increasing from 0.919 for the plate with 20% infill to 0.966 for the fully filled plate.

For illustration, Figure 5 shows the first eight predicted mode shapes of the homogenized plate model with a 20% core infill density, for which a different ordering of some modes was experimentally observed compared with the other core infill densities. The predicted natural frequencies also confirm the small frequency separation between the first and second modes, as well as between the fourth and fifth modes. In the latter case, the calculated natural frequencies are identical (571.4 Hz), indicating a pair of repeated natural frequencies. Such closely spaced or repeated natural frequencies make the ordering

and identification of these modes particularly sensitive to small variations in mechanical properties and boundary conditions.

Table 9. Diagonal MAC values between measured and predicted modal shapes.

	MAC_{rr} [−]								
Core Infill	**1**	**2**	**3**	**4**	**5**	**6**	**7**	**8**	$\overline{MAC}$
20%	0.924	0.963	0.893	0.944	0.935	0.822	0.935	0.936	0.919
40%	0.946	0.932	0.93	0.976	0.882	0.946	0.935	0.868	0.927
60%	0.963	0.961	0.937	0.964	0.931	0.941	0.912	0.822	0.929
80%	0.971	0.958	0.956	0.984	0.958	0.949	0.945	0.908	0.954
100%	0.978	0.961	0.949	0.967	0.982	0.958	0.966	0.968	0.966

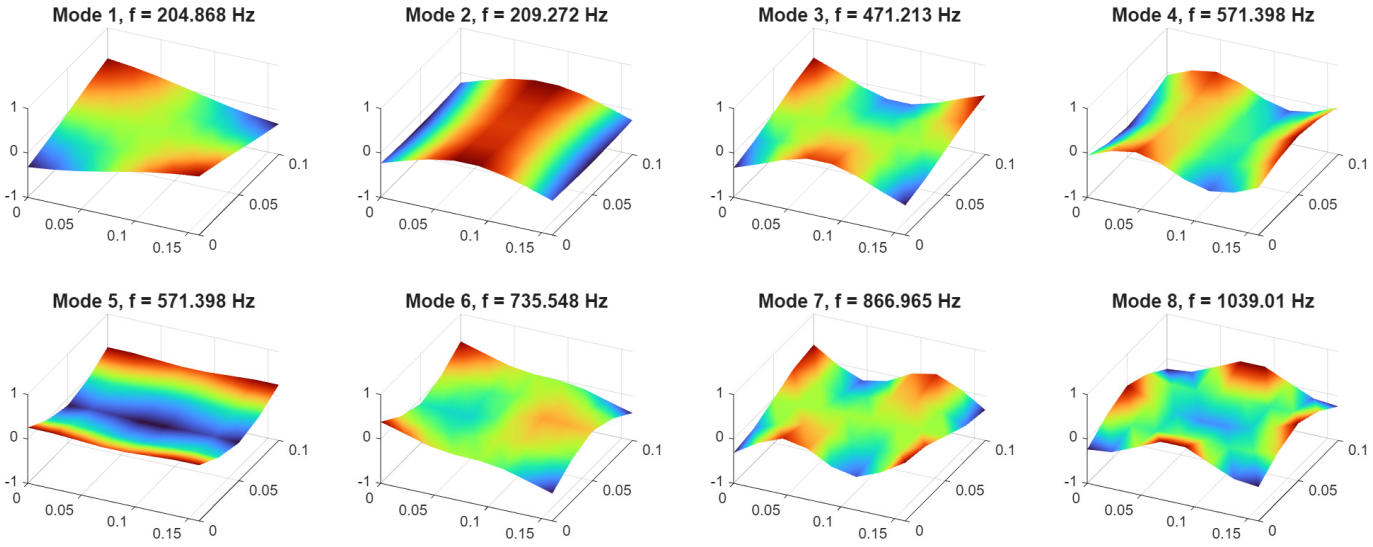

Figure 5. The resulting predicted mode shapes and natural frequencies of the homogenized plate model with 20% core infill.

In this context, the difference between the idealized and experimentally realized boundary conditions should be considered. The homogenized model assumes an ideal free–free plate without any external constraints, whereas in the experimental modal analysis, free–free conditions were only approximated by suspending the plate on elastic cords. Although the natural frequencies of the suspension-related modes satisfied the adopted criterion for quasi-free boundary conditions, the elastic suspension does not represent a completely unconstrained condition. Its influence on the flexible-mode natural frequencies can be considered small given that the quasi-free boundary condition criterion was satisfied. Nevertheless, for modes with very closely spaced or repeated natural frequencies, it cannot be excluded that even such weak coupling may contribute to changes in their frequency separation and frequency-based ordering.

Despite the close frequency spacing of these modes, the predicted mode shapes generally correspond well to those identified experimentally. Their unambiguous pairing is demonstrated by the complete Cross-MAC matrix shown in Figure 6. The relatively high diagonal values, combined with low off-diagonal values not exceeding 0.1, indicate a clear correspondence between the corresponding experimental and predicted mode shapes, while also demonstrating low similarity between non-corresponding modes. A similar pattern of the Cross-MAC matrices was observed for the other analyzed core infill densities.

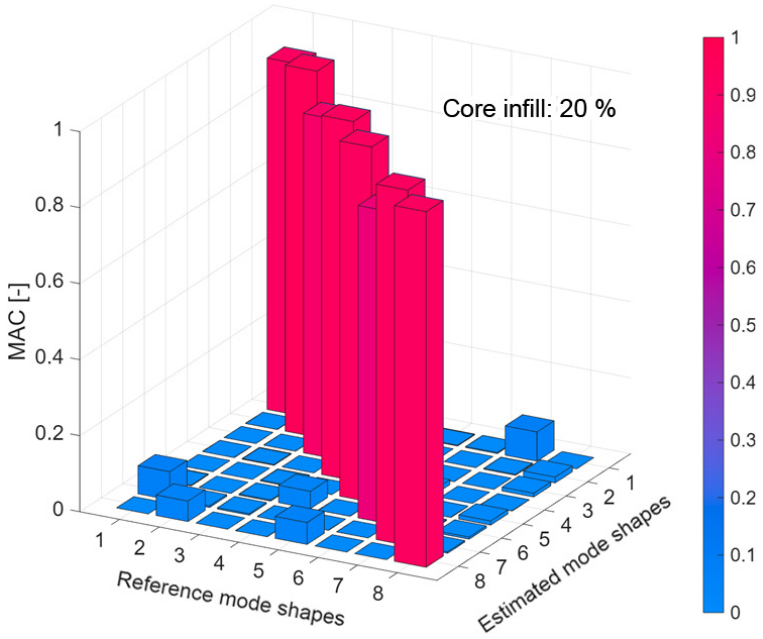

Figure 6. 3D Cross-MAC matrix expressing the agreement between the measured and predicted modal shapes of the plates with 20% core infill.

4. Discussion

The identification results demonstrate a pronounced dependence of the equivalent elastic properties of the homogenized plates on the core infill density. Both Young's modulus and shear modulus increase systematically with increasing infill density, reflecting the greater contribution of the core material to the overall stiffness of the structure. As the core infill density increases from 20% to 100%, the identified Young's modulus increases from 796.1 to 1855 MPa, while the shear modulus increases from 294.4 to 751 MPa. These findings confirm that the core infill density substantially influences both the in-plane normal and shear stiffness characteristics of the homogenized plate.

In contrast, the identified Poisson's ratio exhibits a non-monotonic variation, ranging from 0.296 to 0.414, without a clear dependence on the core infill density. The lowest value is obtained for the plate with 40% infill, whereas the highest corresponds to the plate with 20% infill. At 100% infill, Poisson's ratio reaches 0.384. This behavior suggests that the equivalent transverse deformation response is influenced by the internal lattice geometry and its deformation mechanisms rather than by the core infill density alone.

The high agreement between the experimentally obtained and numerically predicted modal parameters demonstrates the ability of the proposed methodology to reproduce the global dynamic response of the analyzed plates using the identified equivalent material properties. The general increase in MAC values with increasing core infill density may be associated with the mechanical behavior of the discrete lattice structure progressively approaching that of a continuous medium, which forms the basis of the homogenized model. At lower infill densities, the discrete nature of the core and local deformation of individual lattice elements may become more pronounced, leading to local variability in the structural response that cannot be explicitly captured by the homogenized model. This effect may contribute to the lower MAC values observed particularly for the plate with a 20% core infill density.

The simultaneous achievement of low natural frequency deviations and high MAC values indicates that the optimization procedure successfully reproduces both the natural frequencies and their corresponding mode shapes. The remaining discrepancies between the

experimental and predicted modal parameters may be attributed to the homogenization of the discrete lattice structure, manufacturing deviations in the actual specimens, uncertainties associated with the experimental modal analysis, and differences between the ideal free–free boundary conditions assumed in the model and the experimentally realized quasi-free suspension conditions.

The identified elastic constants are directly reflected in the bending stiffness coefficients of the homogenized plates: $D_{11} = D_{22}$, D_{12} and D_{66}. All these coefficients increase with core infill density, reflecting the increasing stiffness of the homogenized structure. Of particular importance is the coefficient D_{66}, which characterizes the twisting stiffness of the plate. In the adopted orthotropic model with square symmetry, the shear modulus G is identified independently of E and ν. Consequently, D_{66} is not constrained by the constitutive relationship, $D_{66,iso} = \frac{1}{2}(D_{11} - D_{12})$, imposed by isotropy. This additional independent parameter enables the homogenized model to account for differences between the bending and twisting stiffness characteristics of the lattice-core structure that cannot be adequately reproduced simultaneously by an isotropic material model.

To quantitatively assess the deviation of the identified twisting stiffness from isotropic behavior, a dimensionless indicator $\eta_{D_{66}}$ was introduced. It relates the coefficient D_{66}, calculated from the identified elastic constants, to its isotropic $D_{66,iso}$ counterpart, i.e.,

$$\eta_{D_{66}} = \frac{D_{66}}{D_{66,iso}} = \frac{2D_{66}}{(D_{11} - D_{12})}, \tag{32}$$

where $\eta_{D_{66}} = 1$ corresponds to the isotropic relation. A value above or below unity directly indicates the extent to which the identified twisting stiffness exceeds or falls below the value predicted by the isotropic constitutive relationship, respectively.

Table 10 presents the values of $\eta_{D_{66}}$ together with the percentage deviation from the isotropic value $D_{66,iso}$, as a function of the plate core infill density. For all five investigated core infill densities, the indicator exceeds unity, demonstrating that the independently identified shear modulus produces a higher twisting stiffness than that predicted by the isotropic relationship using the same identified Young's modulus and Poisson's ratio. The largest deviation is observed at 60% core infill, where the twisting stiffness exceeds its isotropic counterpart by 38.3%. At 20% and 100% infill, the corresponding deviations decrease to approximately 5% and 12%, respectively. These results reveal a non-monotonic dependence of the deviation from isotropic constitutive behavior on core infill density, suggesting that the relative contributions of bending and twisting stiffness are influenced by the deformation mechanisms associated with the internal lattice structure.

Table 10. Twisting stiffness ratio $\eta_{D_{66}}$ and the corresponding deviation from the isotropic constitutive relationship at different core infill densities.

	20%	**40%**	**60%**	**80%**	**100%**
$\eta_{D_{66}}$ [−]	1.046	1.257	1.383	1.340	1.121
Deviation from isotropy [%]	+4.6	+25.7	+38.3	+34.0	+12.1

To further assess the significance of identifying the shear modulus independently, the results obtained using the orthotropic model with square symmetry were compared with those of an isotropic model. For a consistent comparison, the isotropic model was subjected to the same identification procedure, using the same experimental modal data, polynomial basis, and objective-function weighting coefficients. Unlike the orthotropic model, the isotropic formulation contains only two independent elastic constants, since the shear modulus is determined by the relationship $G = \frac{E}{2(1+\nu)}$. The results for both constitutive models are presented in Tables 11 and 12.

Table 11. Comparison of the equivalent material properties of the homogenized plates identified using the orthotropic (square-symmetry) and isotropic models.

Core Infill	E [MPa]	E_{iso} [MPa]	ν [−]	ν_{iso} [−]	G [MPa]	G_{iso} [MPa]
20%	796.1	811.1	0.414	0.408	294.4	288.1
40%	1005	1066	0.296	0.102	487.6	483.4
60%	1099	1240	0.388	0.320	547.7	469.8
80%	1283	1434	0.398	0.326	614.9	540.9
100%	1855	1939	0.384	0.341	751.0	722.7

Table 12. Comparison of the mean absolute relative deviations in natural frequencies and mean MAC values obtained using the orthotropic (square-symmetry) and isotropic models.

Core Infill	$\overline{\Delta f}$ [%]	$\overline{\Delta f}_{iso}$ [%]	$\overline{MAC}$ [−]	$\overline{MAC}_{iso}$ [−]
20%	1.571	1.552	0.919	0.919
40%	1.665	2.181	0.927	0.914
60%	0.758	4.249	0.929	0.706
80%	0.276	3.211	0.954	0.719
100%	0.387	0.805	0.966	0.725

The comparison reveals differences in both the identified equivalent elastic constants and the agreement between the calculated and experimental modal characteristics. In particular, the isotropic model yields different estimates of Young's modulus and Poisson's ratio, reflecting the restrictions imposed by the isotropic constitutive relationship. These differences are most pronounced for the plates with intermediate core infill densities. In addition, the orthotropic model generally provides better agreement with the experimental modal characteristics. The most substantial improvements in natural frequency prediction are observed at core infill densities of 60% and 80%, where the mean absolute relative frequency deviations decrease from 4.249% and 3.211% for the isotropic model to 0.758% and 0.276%, respectively. The mean agreement between the predicted and experimental mode shapes, assessed by the diagonal MAC values, also improves, particularly for the plates with core infill densities of 60%, 80%, and 100%. For these configurations, the isotropic model predicts a reversed frequency-based ordering of the first two flexible modes compared with the experimental reference modes. Consequently, the comparison of corresponding modes based on their frequency order results in lower diagonal MAC values, reflecting the inability of the isotropic model to reproduce the correct mode ordering. At 20% core infill density, both models exhibit comparable performance, indicating that the additional independent elastic constant provides only a limited improvement for this particular configuration.

Overall, the results demonstrate that independently identifying the shear modulus can substantially improve the representation of the global dynamic response of the investigated lattice-core plates, particularly when their equivalent stiffness characteristics deviate from the isotropic constitutive relationship.

To illustrate the practical motivation for the proposed methodology for identifying equivalent material properties, a modal analysis of a detailed finite element model of the plate with 20% core infill was performed using Abaqus 2025 (Dassault Systemes, Vélizy-Villacoublay, France). The objective was to assess the ability of a model based on nominal geometric and material parameters to reproduce the experimentally determined dynamic characteristics of the actual 3D-printed plate.

Unlike the homogenized model, the plate was represented by a three-dimensional shell model explicitly incorporating the face sheets, lattice core, and peripheral frame. The geometry was based on the nominal plate dimensions and 3D printing parameters shown in

Figure 1, while a lattice wall thickness of 0.42 mm and wall spacing of 4.8 mm were verified by measurements on the manufactured specimen. An isotropic linear elastic material model was employed, with Young's modulus and Poisson's ratio defined according to the nominal properties of the base material listed in Table 1. The material density was adjusted to 942 kg/m^3 to match the actual specimen mass of 30.5 g. The finite element mesh consisted of 49,904 four-node shell elements (S4R) and 370 three-node shell elements (S3), with an average element size of 1 mm. The modal analysis was performed under free–free boundary conditions. The model geometry, a partial view of the internal structure, and the finite element mesh are shown in Figure 7.

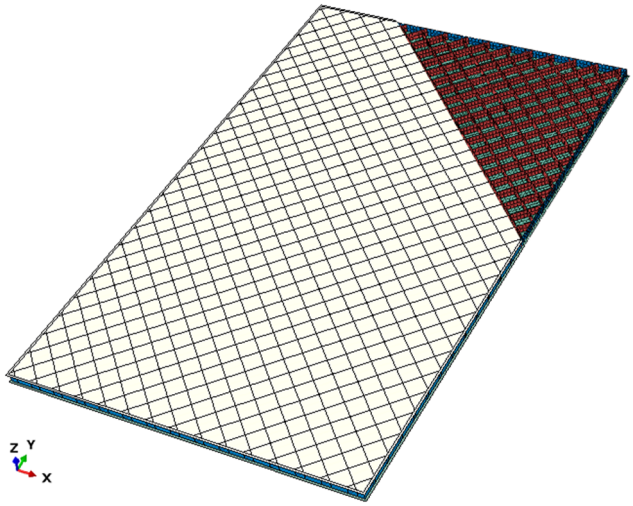

Figure 7. Shell model of a plate with 20% core infill, a partial view of the internal structure and the finite element mesh.

The comparison of the first eight natural frequencies in Table 13 reveals a systematic overestimation of the experimental values by approximately 23–27%, with a mean absolute relative deviation of approximately 25%. Despite the detailed geometric representation and agreement in total mass, the model fails to accurately reproduce the measured dynamic response. These discrepancies may arise from differences between nominal and actual material properties, manufacturing-induced geometric deviations, or idealizations of the connections between structural components.

Table 13. Comparison of the natural frequencies of the nominal FEM model of a plate with 20% core fill and the experimentally determined values for the actual plate.

Mode	1	2	3	4	5	6	7	8
f_{EMA} [Hz]	210.8	216.0	468.7	566.3	574.0	719.5	855.8	1027
f_{FEM} [Hz]	262.5	270.1	592.7	704.5	721.0	895.5	1066	1261
Δf [%]	+24.6	+25.0	+26.5	+24.4	+25.6	+24.5	+24.6	+22.8

This result demonstrates that a geometrically detailed finite element model based on nominal manufacturing and material parameters, without calibration, does not necessarily ensure an accurate prediction of the dynamic behavior of 3D-printed lattice structures. Moreover, explicitly modeling the internal geometry requires considerable modeling effort and increases computational demands. The proposed modal-based identification methodology provides an alternative approach by determining equivalent elastic properties from experimentally measured dynamic characteristics, enabling the global dynamic response to be reproduced using a substantially simpler homogenized model.

To assess the computational efficiency of the proposed methodology for identifying equivalent elastic constants, a comparison was performed with an FE model updating approach based on repeated finite element modal analyses. A simplified homogeneous shell model of the plate with 20% core infill was developed in Abaqus 2025, with dimensions of 100 × 160 mm, a thickness of 4 mm, and an equivalent density of 476.6 kg/m^3 corresponding to the experimentally determined value reported in Table 7. The finite element mesh consisted of 4000 four-node S4R shell elements with an element size of 2 mm. An isotropic linear elastic material model was adopted, with the initial values of Young's modulus and Poisson's ratio taken from Table 1. The isotropic assumption was selected based on the preceding results, which indicated that the plate with 20% infill exhibited the smallest deviation from isotropic constitutive behavior.

The identification of material parameters was performed in Isight 2025 (Dassault Systemes, Vélizy-Villacoublay, France) by optimizing Young's modulus E and Poisson's ratio ν to minimize the differences between the numerically predicted and experimentally determined natural frequencies of the first eight flexible modes. The NLPQLP (Sequential Quadratic Programming) algorithm was employed with a Relative Step Size of 0.05, while the remaining settings were kept at their default values. The optimization workflow, consisting of the optimization module and the modal analysis performed in Abaqus, is illustrated in Figure 8.

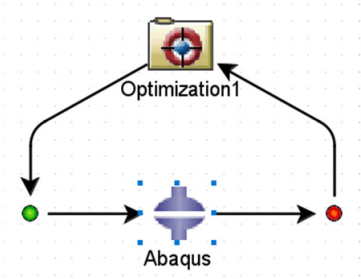

Figure 8. Flowchart of the optimization procedure in Isight.

The optimization was completed after 47 computational steps, with the lowest objective function value obtained at step 28. The identified parameters were $E = 824.3$ MPa and $\nu = 0.353$, corresponding to a shear modulus of $G = 304.6$ MPa under the isotropic assumption. Compared with the orthotropic model identified in MATLAB, the values of E and G were approximately 3.5% higher, while Poisson's ratio was 14.7% lower. The mean absolute relative deviation between the predicted and experimentally measured natural frequencies of the first eight modes was 0.74%. The optimization was based exclusively on natural frequencies, without quantitative evaluation of mode shape agreement. Nevertheless, visual inspection confirmed that the predicted mode shapes followed the same modal sequence as the experimental results.

The total computational time of the FE model updating procedure was approximately 18 min, whereas identification using the proposed methodology in MATLAB required approximately 10 s on the same computer. This represents a substantial reduction in computational time. A comparison of the identified elastic constants, frequency prediction accuracy, and computational time for both approaches is presented in Table 14. Despite the excellent frequency agreement achieved by the optimized FE model, these results demonstrate the substantially lower computational cost of the proposed modal-based identification approach. However, the observed difference in computational time reflects the specific implementations of the two identification procedures and depends not only on

the underlying numerical models but also on the optimization algorithms, their settings, number of objective function evaluations, etc.

Table 14. Comparison of equivalent elastic constants, natural frequency prediction accuracy, and normalized computational time obtained using FE model updating (Isight) and the proposed modal-based identification method (MATLAB).

Solver	Material Model	E [MPa]	ν [–]	G [MPa]	$\overline{\Delta f}$ [%]	Normalized Computation Time
Isight	Isotropic	824.3	0.353	304.6	0.74	108
MATLAB	Orthotropic	796.1	0.414	294.4	1.57	1

5. Conclusions

This study presented a modal-based methodology for identifying the equivalent material properties of 3D-printed lattice-core plates with different core infill densities. The discrete plate structure was replaced by a homogenized orthotropic model with square symmetry, characterized by three independent elastic constants: Young's modulus E, shear modulus G, and Poisson's ratio ν. These parameters were identified by minimizing discrepancies between experimentally determined and numerically predicted natural frequencies and mode shapes, with the latter evaluated using the Ritz method.

The results demonstrated a pronounced dependence of the identified equivalent elastic properties on the core infill density. As the nominal infill density increased from 20% to 100%, Young's modulus increased from approximately 796 to 1855 MPa, while the shear modulus increased from 294 to 751 MPa. In contrast, Poisson's ratio exhibited a non-monotonic variation between 0.296 and 0.414. The identified parameters enabled the global dynamic response of the investigated plates to be reproduced with high accuracy. The mean absolute relative deviation of the natural frequencies of the first eight flexible modes ranged from 0.28% to 1.67%, while the mean diagonal MAC values ranged from 0.919 to 0.966 across the five investigated infill densities.

An important finding concerns the independent identification of the shear modulus and its influence on the twisting stiffness of the homogenized plate. The dimensionless twisting stiffness ratio, $\eta_{D_{66}}$ introduced, exceeded unity for all investigated infill densities, indicating that the identified twisting stiffness was higher than its isotropic counterpart calculated using the same Young's modulus and Poisson's ratio. The deviation ranged from 4.6% to 38.3%, reaching its maximum at 60% infill. The non-monotonic variation in this ratio demonstrates that the deviation from isotropic constitutive behavior cannot be characterized by core infill density alone.

The comparison with independently optimized isotropic models further confirmed the importance of treating the shear modulus as an independent parameter. The orthotropic formulation generally provided better agreement with the experimental modal characteristics, particularly at intermediate infill densities. At 60% and 80% infill, the mean absolute relative frequency deviations decreased from 4.25% and 3.21% for the isotropic models to 0.76% and 0.28%, respectively. Moreover, the orthotropic models reproduced the experimentally observed ordering of the first two flexible modes, which was reversed by the isotropic models at 60%, 80%, and 100% infill. These findings demonstrate the benefit of the additional independent elastic constant for representing the global dynamic behavior of lattice-core plates whose equivalent stiffness characteristics deviate from isotropy.

The practical motivation for experiment-informed identification was illustrated by a detailed finite element model of the plate with 20% infill. Despite explicitly representing the lattice geometry and matching the specimen mass, the model based on nominal material properties overestimated the measured natural frequencies by approximately 25% on

average. This result highlights the limitations of relying solely on nominal material and manufacturing parameters when predicting the dynamic behavior of 3D-printed lattice structures. A separate comparison with an optimized homogeneous FE model demonstrated that FE model updating can also achieve high frequency prediction accuracy, with a mean absolute relative deviation of 0.74%. However, the FE-based identification required 108 times longer in computational time than the proposed MATLAB implementation on the same computer. This substantial difference illustrates the computational efficiency of the proposed methodology, although the comparison also reflects differences in the numerical models, optimization algorithms, and identification criteria.

From a practical perspective, the proposed approach enables experimentally characterized lattice-core plates to be represented by simplified continuum models with a small set of equivalent elastic constants, avoiding the need to explicitly model the internal lattice geometry in subsequent global structural analyses. The identified properties are intended to reproduce the overall elastic and dynamic response within the investigated modeling assumptions rather than local deformation mechanisms of individual lattice elements. Further research should examine the transferability of the methodology to other lattice geometries, material systems, and structural configurations, as well as the influence of manufacturing variability on the identified equivalent properties.

Supplementary Materials: The following supporting information can be downloaded at https://www.mdpi.com/article/10.3390/jcs10110623/s1. equivalent_properties_identification.m: MATLAB script for identification of equivalent material properties of the homogenized 3D-printed plates with lattice cores.

Author Contributions: Conceptualization, R.H. and M.F.; methodology, R.H. and M.H.; software, R.H. and M.H.; investigation, P.P.; resources, M.F.; data curation, P.P.; validation, M.H.; formal analysis, P.P. and M.F.; writing—original draft preparation, R.H., M.F. and M.H.; writing—review and editing, R.H. and M.H.; visualization, P.P.; supervision, M.H.; funding acquisition, R.H. and M.H. All authors have read and agreed to the published version of the manuscript.

Funding: This research was funded by the Slovak Research and Development Agency, grant number APVV-23-0461 "Design and research of mechanical properties of structured materials", by the Scientific Grant Agency of the Ministry of Education, Research, Development and Youth of the Slovak Republic and the Slovak Academy of Sciences under the contract No. VEGA 1/0292/26 "Development of non-traditional experimental methods for evaluation of mechanical and modal properties of metamaterials", and by the project No. CZ.02.01.01/00/22_008/0004631 "Materials and technologies for sustainable development" within the Jan Amos Komensky Operational Program financed by the European Union and from the state budget of the Czech Republic.

Institutional Review Board Statement: Not applicable.

Data Availability Statement: The raw data supporting the conclusions of this article will be made available by the authors on request.

Acknowledgments: During the preparation of this manuscript, the authors utilized ChatGPT (GPT-5.6, OpenAI) to assist with MATLAB code development and improve text clarity and grammar. The methodology development, mathematical formulations, and code validation were conducted solely by the authors. The authors critically evaluated and revised all AI-generated output and assume full responsibility for the accuracy, originality, and integrity of the work.

Conflicts of Interest: The authors declare no conflicts of interest.

Abbreviations

The following abbreviations are used in this manuscript:

PLA	Polylactic Acid
FFF	Fused Filament Fabrication
FDM	Fused Deposition Modeling
LPD	Layer Plastic Deposition
TPMS	Triply Periodic Minimal Surface
RVE	Representative Volume Element
FE	Finite Element
FEMU	Finite Element Model Updating
MAC	Modal Assurance Criterion
RFP-Z	Rational Fraction Polynomial in the Z-domain

References

1. Sola, A.; Chong, W.J.; Pejak Simunec, D.; Li, Y.; Trinchi, A.; Kyratzis, I.L.; Wen, C. Open challenges in tensile testing of additively manufactured polymers: A literature survey and a case study in fused filament fabrication. *Polym. Test.* **2023**, *117*, 107859. [CrossRef]
2. Harpool, T.D.; Alarifi, I.M.; Alshammari, B.A.; Aabid, A.; Baig, M.; Malik, R.A.; Mohamed Sayed, A.; Asmatulu, R.; EL-Bagory, T.M.A.A. Evaluation of the infill design on the tensile response of 3D printed polylactic acid polymer. *Materials* **2021**, *14*, 2195. [CrossRef] [PubMed]
3. Birosz, M.T.; Ledenyák, D.; Andó, M. Effect of FDM infill patterns on mechanical properties. *Polym. Test.* **2022**, *113*, 107654. [CrossRef]
4. Guo, X.; Wang, E.; Yang, H.; Zhai, W. Mechanical characterization and constitutive modeling of additively-manufactured polymeric materials and lattice structures. *J. Mech. Phys. Solids* **2024**, *189*, 105711. [CrossRef]
5. Egan, P.F.; Khatri, N.R.; Parab, M.A.; Arefin, A.M.E. Mechanics of 3D-printed polymer lattices with varied design and processing strategies. *Polymers* **2022**, *14*, 5515. [CrossRef] [PubMed]
6. Sun, Z.P.; Guo, Y.B.; Shim, V.P.W. Deformation and energy absorption characteristics of additively-manufactured polymeric lattice structures—Effects of cell topology and material anisotropy. *Thin-Walled Struct.* **2021**, *169*, 108420. [CrossRef]
7. Munford, M.; Hossain, U.; Ghouse, S.; Jeffers, J.R.T. Prediction of anisotropic mechanical properties for lattice structures. *Addit. Manuf.* **2020**, *32*, 101041. [CrossRef]
8. Wang, Z.; Xu, M.; Du, J.; Jin, Y. Experimental and numerical investigation of polymer-based 3D-printed lattice structures with largely tunable mechanical properties based on triply periodic minimal surface. *Polymers* **2024**, *16*, 711. [CrossRef] [PubMed]
9. Anoop, M.S.; Senthil, P. Homogenisation of elastic properties in FDM components using microscale RVE numerical analysis. *J. Braz. Soc. Mech. Sci. Eng.* **2019**, *41*, 516. [CrossRef]
10. Gonabadi, H.; Chen, Y.; Yadav, A.; Bull, S. Investigation of the effect of raster angle, build orientation, and infill density on the elastic response of 3D printed parts using finite element microstructural modeling and homogenization techniques. *Int. J. Adv. Manuf. Technol.* **2022**, *118*, 1485–1510. [CrossRef]
11. Bhandari, S.; Lopez-Anido, R.A. Finite element analysis of thermoplastic polymer extrusion 3D printed material for mechanical property prediction. *Addit. Manuf.* **2018**, *22*, 187–196. [CrossRef]
12. Bean, P.; Lopez-Anido, R.A.; Vel, S. Numerical modeling and experimental investigation of effective elastic properties of the 3D printed gyroid infill. *Appl. Sci.* **2022**, *12*, 2180. [CrossRef]
13. Monaldo, E.; Marfia, S. Computational homogenization of 3D printed materials by a reduced order model. *Int. J. Mech. Sci.* **2021**, *197*, 106332. [CrossRef]
14. Wu, D.; Mei, Z.; Hu, H.; Zhu, Y. An improved asymptotic homogenization method for vibration analysis of composite sandwich plates with lattice grids. *Compos. Struct.* **2023**, *308*, 116629. [CrossRef]
15. Guan, C.; Lou, R.; Chen, Y.; Qin, C.; Shi, Z.; Liang, L.; Li, H. A homogenization method for natural frequencies and damping of sandwich panels based on representative volume elements. *Compos. Struct.* **2024**, *329*, 117740. [CrossRef]
16. Guan, C.; Tang, Z.-J.; Zhao, F.; Yang, Z.; Li, H. A homogenization method for natural frequencies and damping analysis of composite pyramidal lattice truss sandwich structures based on representative volume elements. *J. Sandw. Struct. Mater.* **2023**, *25*, 572–590. [CrossRef]
17. Nguyen, H.T.; Crittenden, K.; Weiss, L.; Bardaweel, H. Experimental modal analysis and characterization of additively manufactured polymers. *Polymers* **2022**, *14*, 2071. [CrossRef] [PubMed]
18. Baran, T. Free Vibration Analysis of Non-Uniform Timoshenko Beams Using Haar Wavelets. *Rev. Int. Métod. Numér. Cálc. Diseño Ing.* **2024**, *40*, 46. [CrossRef]

19. Ablitzer, F.; Pézerat, C.; Lascoup, B.; Brocail, J. Identification of the flexural stiffness parameters of an orthotropic plate from the local dynamic equilibrium without a priori knowledge of the principal directions. *J. Sound Vib.* **2017**, *404*, 31–46. Correction in *J. Sound Vib.* **2019**, *438*, 382. [CrossRef]
20. Battaglia, G.; Di Matteo, A.; Micale, G.; Pirrotta, A. Vibration-based identification of mechanical properties of orthotropic arbitrarily shaped plates: Numerical and experimental assessment. *Compos. Part B Eng.* **2018**, *150*, 212–225. [CrossRef]
21. De Nunzio, A.V.; Nobile, R.; Faraco, G.; Messina, A. Experimental validation of an innovative inverse material constants identification method based on natural frequencies. *Compos. Struct.* **2025**, *372*, 119540. [CrossRef]
22. Tam, J.H.; Ong, Z.C.; Ismail, Z.; Ang, B.C.; Khoo, S.Y. Inverse identification of composite material properties by using a two-stage Fourier method. *Exp. Mech.* **2018**, *58*, 963–981. [CrossRef]
23. Bui, T.A.; Lardeur, P.; Oudjène, M.; Park, J. A fast and efficient pseudo-direct identification method for orthotropic elastic properties of multi-layered composite plates. *Compos. Struct.* **2024**, *331*, 118369. [CrossRef]
24. Ragauskas, P.; Jasevičius, R. Objective function distortion reduction in identification technique of composite material elastic properties. *Vibration* **2024**, *7*, 177–195. [CrossRef]
25. Cuadrado, M.; Artero-Guerrero, J.A.; Pernas-Sánchez, J.; Varas, D. Model updating of uncertain parameters of carbon/epoxy composite plates from experimental modal data. *J. Sound Vib.* **2019**, *455*, 380–401. [CrossRef]
26. Viala, R.; Placet, V.; Cogan, S. Identification of the anisotropic elastic and damping properties of complex shape composite parts using an inverse method based on finite element model updating and 3D velocity fields measurements (FEMU-3DVF): Application to bio-based composite violin soundboards. *Compos. Part A Appl. Sci. Manuf.* **2018**, *106*, 91–103. [CrossRef]
27. Zhang, J.; Lu, L.; Feng, P.; Zhu, T. Nominal elastic modulus assessment in 3D-printed components under varying printing parameters using Bayesian methods and random forest surrogate modeling. *PLoS ONE* **2025**, *20*, e0338204. [CrossRef] [PubMed]
28. Zortrax. *Z-ULTRAT Technical Data Sheet*; Zortrax S.A: Olsztyn, Poland, 2024; Available online: https://zortrax.com (accessed on 24 August 2026).
29. Raoult, A. Symmetry groups in nonlinear elasticity: An exercise in vintage mathematics. *Commun. Pure Appl. Anal.* **2009**, *8*, 435–456. [CrossRef]
30. Reddy, J.N. *Mechanics of Laminated Composite Plates and Shells: Theory and Analysis*, 2nd ed.; CRC Press: Boca Raton, FL, USA, 2003.
31. Grigorenko, Y.M.; Grigorenko, A.Y.; Efimova, T.L. Spline-based investigation of natural vibrations of orthotropic rectangular plates of variable thickness within classical and refined theories. *J. Mech. Mater. Struct.* **2008**, *3*, 929–952. [CrossRef]
32. Kumar, K.D. Free vibration analysis of orthotropic rectangular plates using the Ritz numerical method. *Adv. Eng. Lett.* **2023**, *2*, 143–150. [CrossRef]
33. Hurlebaus, S. Calculation of eigenfrequencies for rectangular free orthotropic plates—An overview. *ZAMM J. Appl. Math. Mech.* **2007**, *87*, 762–772. [CrossRef]
34. Shen, J.; Tang, T.; Wang, L.-L. *Spectral Methods: Algorithms, Analysis and Applications*; Springer Series in Computational Mathematics; Springer: Berlin/Heidelberg, Germany, 2011; Volume 41. [CrossRef]
35. Li, Q.; Huang, W.; Sanchez, J.; Wang, P.; Ding, Q.; Wang, J. Free vibration analysis of rectangular plate with cutouts under elastic boundary conditions in independent coordinate coupling method. *Comput. Model. Eng. Sci.* **2023**, *134*, 2093–2121. [CrossRef]
36. Allemang, R.J. The Modal Assurance Criterion—Twenty Years of Use and Abuse. *Sound Vib.* **2003**, *37*, 14–23.
37. Nelder, J.A.; Mead, R. A simplex method for function minimization. *Comput. J.* **1965**, *7*, 308–313. [CrossRef]

Disclaimer/Publisher's Note: The statements, opinions and data contained in all publications are solely those of the individual author(s) and contributor(s) and not of MDPI and/or the editor(s). MDPI and/or the editor(s) disclaim responsibility for any injury to people or property resulting from any ideas, methods, instructions or products referred to in the content.